Inclusive cross section and single transverse spin asymmetry for very forward neutron production in polarized $p + p$ collisions at $\sqrt{s} = 200$ GeV

A. Adare,[13] S. Afanasiev,[29] C. Aidala,[40,41] N. N. Ajitanand,[59] Y. Akiba,[53,54] H. Al-Bataineh,[47] J. Alexander,[59] K. Aoki,[33,53] L. Aphecetche,[61] J. Asai,[53] E. T. Atomssa,[34] R. Averbeck,[60] T. C. Awes,[49] B. Azmoun,[8] V. Babintsev,[23] M. Bai,[7] G. Baksay,[19] L. Baksay,[19] A. Baldisseri,[16] K. N. Barish,[9] P. D. Barnes,[37,*] B. Bassalleck,[46] A. T. Basye,[1] S. Bathe,[6,9] S. Batsouli,[49] V. Baublis,[52] C. Baumann,[42] A. Bazilevsky,[8] S. Belikov,[8,*] R. Bennett,[60] A. Berdnikov,[56] Y. Berdnikov,[56] A. A. Bickley,[13] J. G. Boissevain,[37] H. Borel,[16] K. Boyle,[60] M. L. Brooks,[37] H. Buesching,[8] V. Bumazhnov,[23] G. Bunce,[8,54] S. Butsyk,[37] C. M. Camacho,[37] S. Campbell,[60] B. S. Chang,[69] W. C. Chang,[2] J.-L. Charvet,[16] S. Chernichenko,[23] C. Y. Chi,[14] M. Chiu,[24] I. J. Choi,[69] R. K. Choudhury,[5] T. Chujo,[64] P. Chung,[59] A. Churyn,[23] V. Cianciolo,[49] Z. Citron,[60] B. A. Cole,[14] P. Constantin,[37] M. Csanád,[18] T. Csörgő,[68] T. Dahms,[60] S. Dairaku,[33,53] K. Das,[20] G. David,[8] A. Denisov,[23] D. d'Enterria,[34] A. Deshpande,[54,60] E. J. Desmond,[8] O. Dietzsch,[57] A. Dion,[60] M. Donadelli,[57] O. Drapier,[34] A. Drees,[60] K. A. Drees,[7] A. K. Dubey,[67] A. Durum,[23] D. Dutta,[5] V. Dzhordzhadze,[9] Y. V. Efremenko,[49] F. Ellinghaus,[13] T. Engelmore,[14] A. Enokizono,[36] H. En'yo,[53,54] S. Esumi,[64] K. O. Eyser,[9] B. Fadem,[43] D. E. Fields,[46,54] M. Finger,[10] M. Finger, Jr.,[10] F. Fleuret,[34] S. L. Fokin,[32] Z. Fraenkel,[67,*] J. E. Frantz,[48,60] A. Franz,[8] A. D. Frawley,[20] K. Fujiwara,[53] Y. Fukao,[33,53] T. Fusayasu,[45] I. Garishvili,[62] A. Glenn,[13] H. Gong,[60] M. Gonin,[34] J. Gosset,[16] Y. Goto,[53,54] R. Granier de Cassagnac,[34] N. Grau,[3,14] S. V. Greene,[65] M. Grosse Perdekamp,[24,54] T. Gunji,[12] H.-Å. Gustafsson,[39,*] A. Hadj Henni,[61] J. S. Haggerty,[8] H. Hamagaki,[12] R. Han,[51] E. P. Hartouni,[36] K. Haruna,[22] E. Haslum,[39] R. Hayano,[12] X. He,[21] M. Heffner,[36] T. K. Hemmick,[60] T. Hester,[9] J. C. Hill,[27] M. Hohlmann,[19] W. Holzmann,[59] K. Homma,[22] B. Hong,[31] T. Horaguchi,[12,53,63] D. Hornback,[62] S. Huang,[65] T. Ichihara,[53,54] R. Ichimiya,[53] H. Iinuma,[33,53] Y. Ikeda,[64] K. Imai,[28,33,53] J. Imrek,[17] M. Inaba,[64] D. Isenhower,[1] M. Ishihara,[53] T. Isobe,[12,53] M. Issah,[59] A. Isupov,[29] D. Ivanischev,[52] B. V. Jacak,[60,†] J. Jia,[14] J. Jin,[14] B. M. Johnson,[8] K. S. Joo,[44] D. Jouan,[50] F. Kajihara,[12] S. Kametani,[53] N. Kamihara,[54] J. Kamin,[60] J. H. Kang,[69] J. Kapustinsky,[37] D. Kawall,[40,54] A. V. Kazantsev,[32] T. Kempel,[27] A. Khanzadeev,[52] K. M. Kijima,[22] J. Kikuchi,[66] B. I. Kim,[31] D. H. Kim,[44] D. J. Kim,[69] E. Kim,[58] S. H. Kim,[69] E. Kinney,[13] K. Kiriluk,[13] Á. Kiss,[18] E. Kistenev,[8] J. Klay,[36] C. Klein-Boesing,[42] L. Kochenda,[52] B. Komkov,[52] M. Konno,[64] J. Koster,[24] A. Kozlov,[67] A. Král,[15] A. Kravitz,[14] G. J. Kunde,[37] K. Kurita,[53,55] M. Kurosawa,[53] M. J. Kweon,[31] Y. Kwon,[62] G. S. Kyle,[47] R. Lacey,[59] Y. S. Lai,[14] J. G. Lajoie,[27] D. Layton,[24] A. Lebedev,[27] D. M. Lee,[37] K. B. Lee,[31] T. Lee,[58] M. J. Leitch,[37] M. A. L. Leite,[57] B. Lenzi,[57] X. Li,[11] P. Liebing,[54] T. Liška,[15] A. Litvinenko,[29] H. Liu,[47] M. X. Liu,[37] B. Love,[65] D. Lynch,[8] C. F. Maguire,[65] Y. I. Makdisi,[7] A. Malakhov,[29] M. D. Malik,[46] V. I. Manko,[32] E. Mannel,[14] Y. Mao,[51,53] L. Mašek,[10,26] H. Masui,[64] F. Matathias,[14] M. McCumber,[60] P. L. McGaughey,[37] N. Means,[60] B. Meredith,[24] Y. Miake,[64] P. Mikeš,[26] K. Miki,[64] A. Milov,[8] M. Mishra,[4] J. T. Mitchell,[8] A. K. Mohanty,[5] Y. Morino,[12] A. Morreale,[9] D. P. Morrison,[8] T. V. Moukhanova,[32] D. Mukhopadhyay,[65] J. Murata,[53,55] S. Nagamiya,[30] J. L. Nagle,[13] M. Naglis,[67] M. I. Nagy,[18] I. Nakagawa,[53,54] Y. Nakamiya,[22] T. Nakamura,[22] K. Nakano,[53,63] J. Newby,[36] M. Nguyen,[60] T. Niida,[64] R. Nouicer,[8] A. S. Nyanin,[32] E. O'Brien,[8] S. X. Oda,[12] C. A. Ogilvie,[27] M. Oka,[64] K. Okada,[54] Y. Onuki,[53] A. Oskarsson,[39] M. Ouchida,[22] K. Ozawa,[12] R. Pak,[8] A. P. T. Palounek,[37] V. Pantuev,[25,60] V. Papavassiliou,[47] J. Park,[58] W. J. Park,[31] S. F. Pate,[47] H. Pei,[27] J.-C. Peng,[24] H. Pereira,[16] V. Peresedov,[29] D. Yu. Peressounko,[32] C. Pinkenburg,[8] M. L. Purschke,[8] A. K. Purwar,[37] H. Qu,[21] J. Rak,[46] A. Rakotozafindrabe,[34] I. Ravinovich,[67] K. F. Read,[49,62] S. Rembeczki,[19] K. Reygers,[42] V. Riabov,[52] Y. Riabov,[52] D. Roach,[65] G. Roche,[38] S. D. Rolnick,[9] M. Rosati,[27] S. S. E. Rosendahl,[39] P. Rosnet,[38] P. Rukoyatkin,[29] P. Ružička,[26] V. L. Rykov,[53] B. Sahlmueller,[42,60] N. Saito,[33,53,54] T. Sakaguchi,[8] S. Sakai,[64] K. Sakashita,[53,63] V. Samsonov,[52] T. Sato,[64] S. Sawada,[30] K. Sedgwick,[9] J. Seele,[13] R. Seidl,[24] A. Yu. Semenov,[27] V. Semenov,[23] R. Seto,[9] D. Sharma,[67] I. Shein,[23] T.-A. Shibata,[53,63] K. Shigaki,[22] M. Shimomura,[64] K. Shoji,[33,53] P. Shukla,[5] A. Sickles,[8] C. L. Silva,[57] D. Silvermyr,[49] C. Silvestre,[16] K. S. Sim,[31] B. K. Singh,[4] C. P. Singh,[4] V. Singh,[4] M. Slunečka,[10] A. Soldatov,[23] R. A. Soltz,[36] W. E. Sondheim,[37] S. P. Sorensen,[62] I. V. Sourikova,[8] F. Staley,[16] P. W. Stankus,[49] E. Stenlund,[39] M. Stepanov,[47] A. Ster,[68] S. P. Stoll,[8] T. Sugitate,[22] C. Suire,[50] A. Sukhanov,[8] J. Sziklai,[68] E. M. Takagui,[57] A. Taketani,[53,54] R. Tanabe,[64] Y. Tanaka,[45] K. Tanida,[53,54,58] M. J. Tannenbaum,[8] A. Taranenko,[59] P. Tarján,[17] H. Themann,[60] T. L. Thomas,[46] M. Togawa,[33,53] A. Toia,[60] L. Tomášek,[26] Y. Tomita,[64] H. Torii,[22,53] R. S. Towell,[1] V-N. Tram,[34] I. Tserruya,[67] Y. Tsuchimoto,[22] C. Vale,[27] H. Valle,[65] H. W. van Hecke,[37] A. Veicht,[24] J. Velkovska,[65] R. Vértesi,[17] A. A. Vinogradov,[32] M. Virius,[15] V. Vrba,[26] E. Vznuzdaev,[52] X. R. Wang,[47] Y. Watanabe,[53,54] F. Wei,[27] J. Wessels,[42] S. N. White,[8] D. Winter,[14] C. L. Woody,[8] M. Wysocki,[13] W. Xie,[54] Y. L. Yamaguchi,[66] K. Yamaura,[22] R. Yang,[24] A. Yanovich,[23] J. Ying,[21] S. Yokkaichi,[53,54] G. R. Young,[49] I. Younus,[35,46] I. E. Yushmanov,[32] W. A. Zajc,[14] O. Zaudtke,[42] C. Zhang,[49] S. Zhou,[11] and L. Zolin[29]

(PHENIX Collaboration)

[1]*Abilene Christian University, Abilene, Texas 79699, USA*
[2]*Institute of Physics, Academia Sinica, Taipei 11529, Taiwan*
[3]*Department of Physics, Augustana College, Sioux Falls, South Dakota 57197, USA*
[4]*Department of Physics, Banaras Hindu University, Varanasi 221 005, India*
[5]*Bhabha Atomic Research Centre, Bombay 400 085, India*
[6]*Baruch College, City University of New York, New York, New York 10010, USA*
[7]*Collider-Accelerator Department, Brookhaven National Laboratory, Upton, New York 11973-5000, USA*
[8]*Physics Department, Brookhaven National Laboratory, Upton, New York 11973-5000, USA*
[9]*University of California, Riverside, Riverside, California 92521, USA*
[10]*Charles University, Ovocný trh 5, Praha 1, 116 36 Prague, Czech Republic*
[11]*Science and Technology on Nuclear Data Laboratory, China Institute of Atomic Energy, Beijing 102413, People's Republic of China*
[12]*Center for Nuclear Study, Graduate School of Science, University of Tokyo, 7-3-1 Hongo, Bunkyo, Tokyo 113-0033, Japan*
[13]*University of Colorado, Boulder, Colorado 80309, USA*
[14]*Columbia University, New York, New York 10027 USA and Nevis Laboratories, Irvington, New York 10533, USA*
[15]*Czech Technical University, Zikova 4, 166 36 Prague 6, Czech Republic*
[16]*Dapnia, CEA Saclay, F-91191 Gif-sur-Yvette, France*
[17]*Debrecen University, H-4010 Debrecen, Egyetem tér 1, Hungary*
[18]*ELTE, Eötvös Loránd University, Pázmány P. s. 1/A, H-1117 Budapest, Hungary*
[19]*Florida Institute of Technology, Melbourne, Florida 32901, USA*
[20]*Florida State University, Tallahassee, Florida 32306, USA*
[21]*Georgia State University, Atlanta, Georgia 30303, USA*
[22]*Hiroshima University, Kagamiyama, Higashi-Hiroshima 739-8526, Japan*
[23]*IHEP Protvino, State Research Center of Russian Federation, Institute for High Energy Physics, Protvino 142281, Russia*
[24]*University of Illinois at Urbana-Champaign, Urbana, Illinois 61801, USA*
[25]*Institute for Nuclear Research of the Russian Academy of Sciences, prospekt 60-letiya Oktyabrya 7a, Moscow 117312, Russia*
[26]*Institute of Physics, Academy of Sciences of the Czech Republic, Na Slovance 2, 182 21 Prague 8, Czech Republic*
[27]*Iowa State University, Ames, Iowa 50011, USA*
[28]*Advanced Science Research Center, Japan Atomic Energy Agency,*
2-4 Shirakata Shirane, Tokai-mura, Naka-gun, Ibaraki-ken 319-1195, Japan
[29]*Joint Institute for Nuclear Research, 141980 Dubna, Moscow Region, Russia*
[30]*KEK, High Energy Accelerator Research Organization, Tsukuba, Ibaraki 305-0801, Japan*
[31]*Korea University, Seoul, 136-701, Korea*
[32]*Russian Research Center "Kurchatov Institute", Moscow 123098, Russia*
[33]*Kyoto University, Kyoto 606-8502, Japan*
[34]*Laboratoire Leprince-Ringuet, Ecole Polytechnique, CNRS-IN2P3, Route de Saclay, F-91128 Palaiseau, France*
[35]*Physics Department, Lahore University of Management Sciences, Lahore, Pakistan*
[36]*Lawrence Livermore National Laboratory, Livermore, California 94550, USA*
[37]*Los Alamos National Laboratory, Los Alamos, New Mexico 87545, USA*
[38]*LPC, Université Blaise Pascal, CNRS-IN2P3, Clermont-Ferrand, 63177 Aubiere Cedex, France*
[39]*Department of Physics, Lund University, Box 118, SE-221 00 Lund, Sweden*
[40]*Department of Physics, University of Massachusetts, Amherst, Massachusetts 01003-9337, USA*
[41]*Department of Physics, University of Michigan, Ann Arbor, Michigan 48109-1040, USA*
[42]*Institut für Kernphysik, University of Muenster, D-48149 Muenster, Germany*
[43]*Muhlenberg College, Allentown, Pennsylvania 18104-5586, USA*
[44]*Myongji University, Yongin, Kyonggido 449-728, Korea*
[45]*Nagasaki Institute of Applied Science, Nagasaki-shi, Nagasaki 851-0193, Japan*
[46]*University of New Mexico, Albuquerque, New Mexico 87131, USA*
[47]*New Mexico State University, Las Cruces, New Mexico 88003, USA*
[48]*Department of Physics and Astronomy, Ohio University, Athens, Ohio 45701, USA*
[49]*Oak Ridge National Laboratory, Oak Ridge, Tennessee 37831, USA*
[50]*IPN-Orsay, Universite Paris Sud, CNRS-IN2P3, BP1, F-91406 Orsay, France*
[51]*Peking University, Beijing 100871, People's Republic of China*
[52]*PNPI, Petersburg Nuclear Physics Institute, Gatchina, Leningrad Region 188300, Russia*
[53]*RIKEN Nishina Center for Accelerator-Based Science, Wako, Saitama 351-0198, Japan*
[54]*RIKEN BNL Research Center, Brookhaven National Laboratory, Upton, New York 11973-5000, USA*
[55]*Physics Department, Rikkyo University, 3-34-1 Nishi-Ikebukuro, Toshima, Tokyo 171-8501, Japan*
[56]*Saint Petersburg State Polytechnic University, St. Petersburg 195251, Russia*

[57]Universidade de São Paulo, Instituto de Física, Caixa Postal 66318, São Paulo CEP05315-970, Brazil
[58]Seoul National University, Seoul, Korea
[59]Chemistry Department, Stony Brook University, SUNY, Stony Brook, New York 11794-3400, USA
[60]Department of Physics and Astronomy, Stony Brook University, SUNY, Stony Brook, New York 11794-3400, USA
[61]SUBATECH (Ecole des Mines de Nantes, CNRS-IN2P3, Université de Nantes) BP 20722, 44307 Nantes, France
[62]University of Tennessee, Knoxville, Tennessee 37996, USA
[63]Department of Physics, Tokyo Institute of Technology, Oh-okayama, Meguro, Tokyo 152-8551, Japan
[64]Institute of Physics, University of Tsukuba, Tsukuba, Ibaraki 305, Japan
[65]Vanderbilt University, Nashville, Tennessee 37235, USA
[66]Waseda University, Advanced Research Institute for Science and Engineering, 17 Kikui-cho, Shinjuku-ku, Tokyo 162-0044, Japan
[67]Weizmann Institute, Rehovot 76100, Israel
[68]Institute for Particle and Nuclear Physics, Wigner Research Centre for Physics, Hungarian Academy of Sciences (Wigner RCP, RMKI) H-1525 Budapest 114, P.O. Box 49, Budapest, Hungary
[69]Yonsei University, IPAP, Seoul 120-749, Korea

(Received 17 September 2012; published 8 August 2013)

The energy dependence of the single-transverse-spin asymmetry, A_N, and the cross section for neutron production at very forward angles were measured in the PHENIX experiment at the Relativistic Heavy Ion Collider for polarized $p + p$ collisions at $\sqrt{s} = 200$ GeV. The neutrons were observed in forward detectors covering an angular range of up to 2.2 mrad. We report results for neutrons with a momentum fraction of $x_F = 0.45$ to 1.0. The energy dependence of the measured cross sections were consistent with x_F scaling, compared to measurements by an experiment at the Intersecting Storage Ring, which measured neutron production in unpolarized $p + p$ collisions at $\sqrt{s} = 30.6$–62.7 GeV. The cross sections for large x_F neutron production for $p + p$ collisions, as well as those in $e + p$ collisions measured at the Hadron-Electron Ring Accelerator, are described by a pion exchange mechanism. The observed forward neutron asymmetries were large, reaching $A_N = -0.08 \pm 0.02$ for $x_F = 0.8$; the measured backward asymmetries, for negative x_F, were consistent with zero. The observed asymmetry for forward neutron production is discussed within the pion exchange framework, with interference between the spin-flip amplitude due to the pion exchange and nonflip amplitudes from all Reggeon exchanges. Within the pion exchange description, the measured neutron asymmetry is sensitive to the contribution of other Reggeon exchanges even for small amplitudes.

DOI: 10.1103/PhysRevD.88.032006 PACS numbers: 13.85.Ni, 13.88.+e, 14.20.Dh, 25.75.Dw

I. INTRODUCTION

With the first polarized $p + p$ collisions at $\sqrt{s} = 200$ GeV at the Relativistic Heavy Ion Collider (RHIC), a large single transverse spin asymmetry (A_N) for neutron production in very forward kinematics was discovered by a polarimeter development experiment [1]. That experiment was designed to measure the asymmetry for very forward photons and used an electromagnetic calorimeter. The calorimeter was used to identify neutrons, originally to remove them from the photon data, when a large asymmetry was observed in forward neutrons. The neutron energy resolution was coarse, so no cross section measurement was reported. The discovery inspired the PHENIX experiment to use existing very forward hadronic calorimeters, with additional shower maximum detectors, to measure the neutron transverse asymmetry at the PHENIX interaction point at RHIC with a significantly better neutron energy resolution. Here we report the first measurements of very forward inclusive and semi-inclusive neutron production cross sections at $\sqrt{s} = 200$ GeV and measurements of A_N for forward and backward production with improved neutron energy resolution. The A_N is a left-right asymmetry written as

$$A_N = \frac{d\sigma^{\uparrow} - d\sigma^{\downarrow}}{d\sigma^{\uparrow} + d\sigma^{\downarrow}} \tag{1}$$

for yields observed to the left when facing along the polarized proton's momentum vector, where $d\sigma^{\uparrow}$ ($d\sigma^{\downarrow}$) is the production cross section when the protons are polarized up (down). The A_N with cross section measurements for higher energy $p + p$ collisions provide qualitatively new information toward an understanding of the production mechanism.

Cross sections of inclusive neutron production in unpolarized $p + p$ collisions were measured at the intersecting storage ring (ISR) from $\sqrt{s} = 30.6$ to 62.7 GeV [2,3]. These cross sections have been described using one pion exchange (OPE) models [4–10]. In OPE, the incoming proton emits a pion which scatters on the other proton as shown in Fig. 1. Kinematics of the neutron are characterized by two variables, x_F and p_T, defined by

$$x_F = p_L/p_{L(\max)} = E_n \cos\theta_n / E_p \sim E_n/E_p, \tag{2}$$

*Deceased.
†PHENIX Spokesperson.
jacak@skipper.physics.sunysb.edu

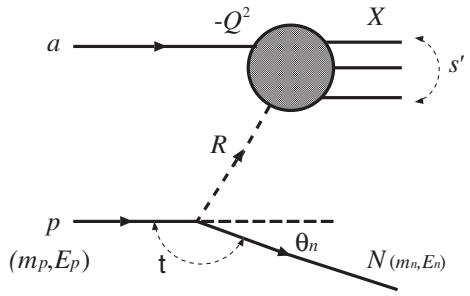

FIG. 1. A schematic diagram of neutron production, $pa \to nX$, for the Reggeon exchange model shown with Lorentz invariant variables s', Q^2, and t. "a" is a proton or positron for $p + p$ or $e^+ p$ reactions. R indicates a Regge trajectory with isospin odd such as π, ρ, a_2, and Pomeron-π in the Regge theory. For pion exchange, $R = \pi$.

$$p_T = E_n \sin\theta_n \sim x_F E_p \theta_n, \tag{3}$$

where p_L is the momentum component of the neutron in the proton-beam direction, E_n and E_p are energies of the neutron and the proton beam, and θ_n is the polar angle of the neutron from the beam direction which is very small ($\sim$ mrad) for forward neutron production. The measured cross section showed a peak around $x_F \sim 0.8$ and was found to have almost no $\sqrt{s}$ dependence. OPE models gave a reasonable description of the data.

OPE models were also used to describe proton and photon induced production of neutrons measured at the Hadron-Electron Ring Accelerator (HERA) $e + p$ collider [11,12]. These measurements probe the pion structure function at small x. The NA49 collaboration also published the cross section for forward neutron production for $p + p$ collisions at $\sqrt{s} = 17.3$ GeV [13]. They compared the result with those from ISR and HERA and found they did not agree.

The neutron asymmetry provides a new tool to probe the production mechanism. For the OPE model, A_N arises from an interference between spin-flip and spin-nonflip amplitudes. Since the pion-exchange amplitude is fully spin-flip, the asymmetry is sensitive to other Reggeon exchange amplitudes which are spin-nonflip, even for small amplitudes.

This paper presents the x_F dependence of cross sections, inclusive and semi-inclusive (with a beam-beam interaction requirement), and A_N for very forward and very backward neutron production in polarized $p + p$ collisions at $\sqrt{s} = 200$ GeV.

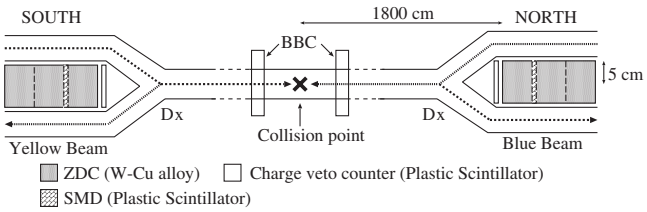

FIG. 2. A plan view of the experimental setup at PHENIX (not to scale). Shown are the principal components for the neutron physics. Charged veto counters are in front of ZDCs, and the SMDs are between the first and second ZDC modules.

II. EXPERIMENTAL SETUP

A. Detector apparatus

A plan view of the experimental setup for very forward neutron measurement at PHENIX [14] is shown in Fig. 2. The RHIC polarized proton beams were vertically polarized. Each collider ring of RHIC was filled with up to 111 bunches in a 120 bunch pattern, spaced 106 ns apart, with predetermined patterns of polarization signs for the bunches. The colliding beam rotating clockwise when viewed from above is referred to as the "blue beam" and the beam rotating counterclockwise the "yellow beam."

Neutrons were measured by a zero-degree calorimeter (ZDC) [15] with a position-sensitive shower-maximum detector (SMD). One ZDC module is composed of Cu-W alloy absorbers with PMMA-based communication grade optical fibers and corresponds to 1.7 nuclear interaction lengths. A single photomultiplier collects Čerenkov light via optical fibers. Three ZDC modules are located in series (5.1 nuclear interaction lengths) at ± 1800 cm away from the collision point, covering 10 cm in the transverse plane.

The SMD comprises x-y scintillator strip hodoscopes and is inserted between the first and second ZDC modules (see Fig. 5 of Ref. [15]) at approximately the depth of the maximum of the hadronic shower. The x coordinate (horizontal) is given by 7 scintillator strips of 15 mm width, while the y coordinate (vertical) is given by 8 strips of 20 mm width, tilted by 45 deg.

The neutron position can be reconstructed from the energy deposited in scintillators with the centroid method. We calculated the centroid:

$$x = \frac{\sum_i^{N_{\text{multi}}^{\text{SMD}}} E(i) \cdot x(i)}{\sum_i^{N_{\text{multi}}^{\text{SMD}}} E(i)}, \tag{4}$$

where $E(i)$ and $x(i)$ are the energy deposit and the position of the ith scintillator, respectively. The number of scintillators with pulse height above the minimum ionization particle peak is shown as $N_{\text{multi}}^{\text{SMD}}$ which is defined as the SMD multiplicity.

Detectors are located downstream of the RHIC dipole (DX) magnet, so that collision-related charged particles are swept out. A forward scintillation counter, with dimensions 10×12 cm, was installed in front of the ZDC to remove charged particle backgrounds from other sources. In this analysis, we used only the south ZDC detector, which is facing the yellow beam.

As a beam luminosity monitor, beam beam counters (BBCs) are used. The BBC comprises 64 photomultiplier tubes and 3 cm thick quartz Čerenkov radiators. The two BBCs are mounted around the beam pipe ± 144 cm away from the collision point which cover $\pm(3.0$–$3.9)$ in pseudorapidity and 2π in azimuth.

The neutron data were collected in 2006 with two triggers. One is the ZDC trigger for neutron inclusive measurements, requiring an energy deposit in the south ZDC greater than 5 GeV. The other trigger was a ZDC ⊗ BBC trigger, a coincidence trigger of the ZDC trigger with BBC hits which are defined as one or more charged particles in both of the BBC detectors. We note that the ZDC trigger was prescaled due to data acquisition limitations. Therefore, the ZDC trigger samples are significantly smaller than the ZDC ⊗ BBC trigger samples.

B. Detector performance

In order to evaluate the detector performance, simulation studies were performed with GEANT3 with GHEISHA [16] which simulated the response of the prototype ZDC to hadrons well. A single neutron event generator and PYTHIA (version 6.220) [17] were used to generate events. The single neutron event generator simulated neutrons as a function of x_F and p_T. The x_F distribution which was used for the simulation input was determined as a differential cross section, $d\sigma/dx_F$, in the cross section analysis (Sec. III A). The p_T distribution is difficult to determine by the PHENIX data alone since the position and energy resolutions are insufficient to adequately determine it, so the p_T distribution from the ISR result, $\exp(-4.8 p_T(\mathrm{GeV}/c))$, was used as simulation input, assuming p_T scaling from the ISR to the PHENIX energies. To check the reliability of this assumption, distributions of radial distance from the detector center, r, for the data and simulation were compared based on the relation of $p_T \propto r$ as

$$p_T = E_n \sin\theta_n = E_n \frac{r}{\sqrt{r^2 + d^2}} \sim E_n \frac{r}{d}, \qquad (5)$$

where d is the distance from the collision point to the detector, corresponding to 1800 cm, and r is determined for the shower centroid with Eq. (4).

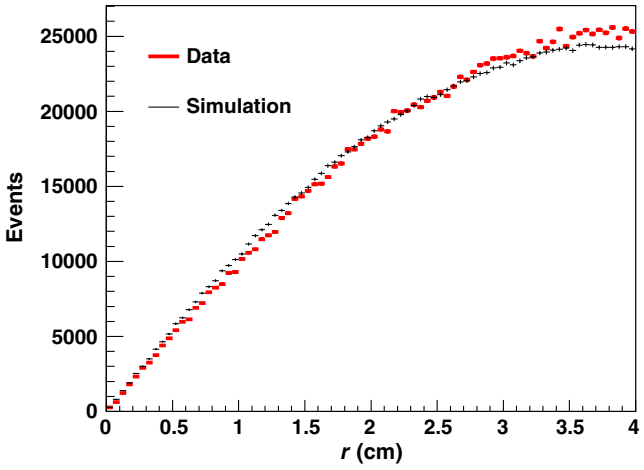

FIG. 3 (color online). r distributions for the data and simulation with the exponential p_T shape. Distributions agreed within $r < 4$ cm.

The comparison of r distributions with the integration of measured ZDC energies 20–120 GeV agreed well as shown in Fig. 3.

1. Performance of the energy measurement

The neutron energy measurement with the ZDC was degraded by a nonlinearity of the photoelectron yield and shower leakage out the back and sides of the detector (edge effect). The ZDC response was studied by simulation with the single neutron event generator.

The energy linearity and resolution were evaluated from the response to incident neutrons with energies from 20 to 100 GeV in the simulation. The absolute scale was normalized at 100 GeV with the experimental data. The ZDC response below 100 GeV exhibits nonlinear behavior as shown in Fig. 4. We applied a correction of the nonlinearity to the experimental data based on this result. We used the difference between the linear and nonlinear response as a component of the systematic uncertainty in the determination of the cross section (Sec. III A).

As shown in Fig. 4, the energy resolution for 20–100 GeV neutrons was described by

$$\frac{\Delta E}{E} = \frac{65\%}{\sqrt{E(\mathrm{GeV})}} + 15\%. \qquad (6)$$

The absolute scale of the energy measurement was normalized with the 100 GeV single neutron peak in heavy ion collisions. However, the energy of neutrons from

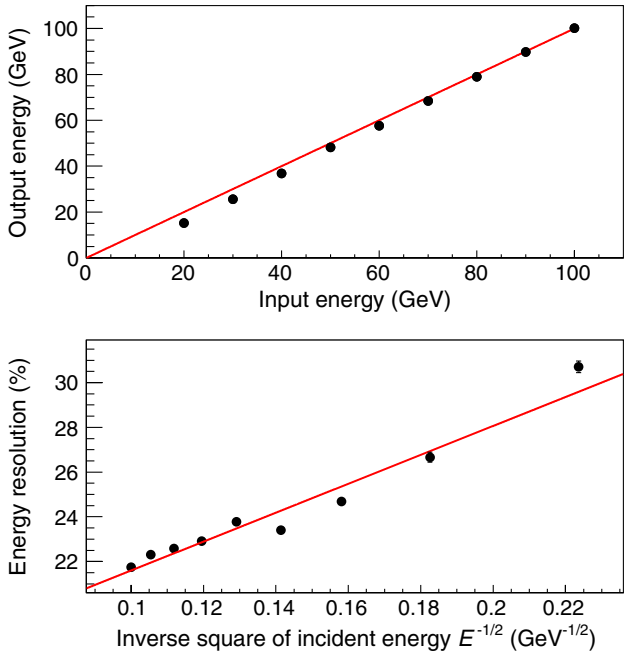

FIG. 4 (color online). (upper) The mean of output energy as a function of the incident neutron energy evaluated by the simulation. The solid line indicates a linear response. (lower) The energy resolution as a function of $1/\sqrt{E}(\mathrm{GeV}^{-1/2})$. The solid line shows the fit result; $\Delta E/E = 65\%/\sqrt{E} + 15\%$.

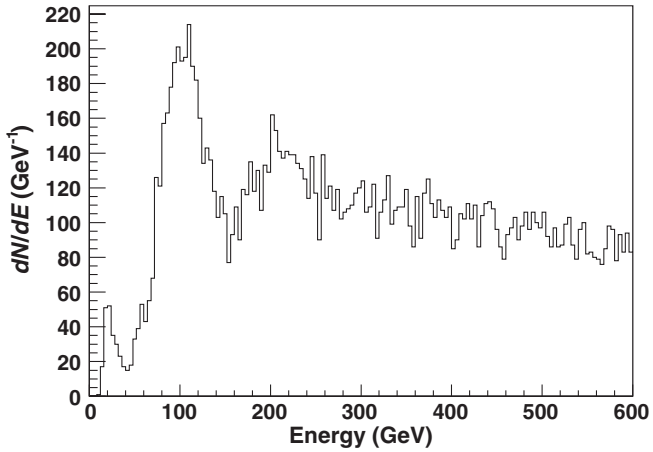

FIG. 5. The energy distribution in the ZDC for Cu + Cu collisions at $\sqrt{s_{NN}} = 200$ GeV. Peripheral events were selected by requiring BBC inactivity.

$p + p$ collisions was below 100 GeV, so simulation was used to estimate the detector response for neutron energies in this region.

Figure 5 shows the absolute energy scale calibrated by observing one neutron from peripheral Cu + Cu collisions at $\sqrt{s_{NN}} = 200$ GeV; 100 GeV neutrons less than 2 mrad from the beam axis produced the single neutron peak. The energy resolution expected from simulation was about 22% for the 100 GeV neutron and was consistent with the observed width of the single neutron peak as shown in Fig. 5. The energy nonlinearity was confirmed by the single neutron peak from Cu + Cu collisions at $\sqrt{s_{NN}} =$ 62.4 GeV shown in Fig. 6 which peaked at 26 ± 0.3 GeV, consistent with nonlinearity indicated by the simulation.

The edge effect was studied by a prototype ZDC with a 100 GeV proton beam at CERN. Generally, the measured energy decreased near the edge; however, nearest the PMT, the measured energy increased. This was found to be

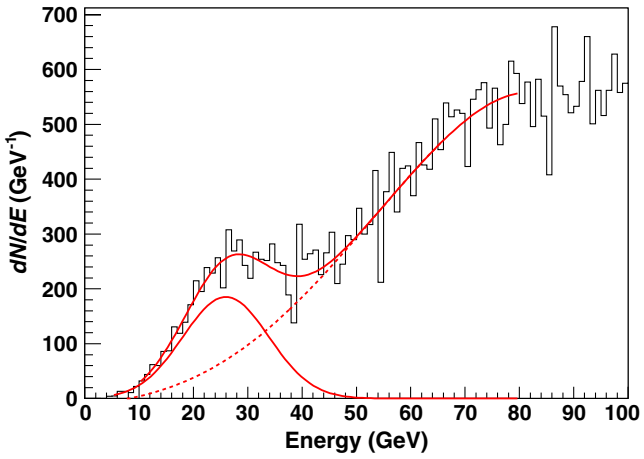

FIG. 6 (color online). The energy distribution in the ZDC for Cu + Cu collision at $\sqrt{s_{NN}} = 62.4$ GeV. The neutron peak position was determined with a Gaussian + polynomial fit.

caused by the fibers in the top region which connected to the PMT (see Fig. 5 of Ref. [15]), where the shower hit the fibers directly. The simulation used to study the prototype reproduced this effect.

A residual edge effect was seen in the data at the top and bottom of the detector, so we chose to apply a fiducial cut to minimize the effect. According to the simulation, 95%–100% of the incident energy was contained within $r < 3$ cm.

2. Performance of the position measurement

The position resolutions were evaluated by the simulation. Figure 7 shows the position resolution (rms) as a function of the neutron incident energy for x (horizontal) and y (vertical) positions. The position resolution was approximately 1 cm for the neutron energy at 100 GeV.

Near the edge of the detector, the position measurement is also affected by shower leakage. If the incident position was in the edge area, the output position was shifted to the detector center due to shower leakage, independent of neutron energy. This position shift caused by the edge effect is corrected based on the simulation.

The reliability of the position measurement was studied by comparing hadron shower shapes of the data and simulation. The shower width and highest shower fraction among all scintillators were calculated for x and y independently. We compared the measured distribution with simulation for each SMD multiplicity since the hadron shower shape sensitively depends on the SMD multiplicity. The distribution of y was well reproduced by the

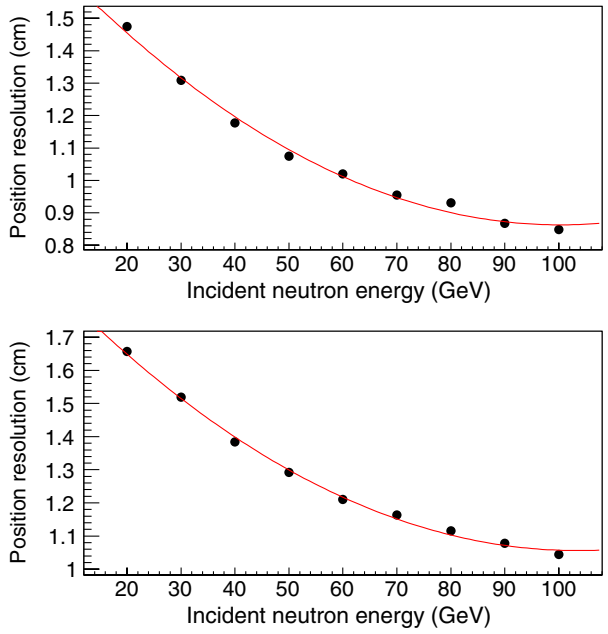

FIG. 7 (color online). The position resolution (rms) as a function of the incident neutron energy for (upper) x and (lower) y. Circles show measured values. They were well reproduced by a second order polynomial fit. Red lines show the fit results.

simulation; however, the distribution of x was not well reproduced, especially for the highest shower fraction in high SMD multiplicity events. The systematic uncertainties for the position measurement were estimated by matching the highest shower fraction of x by smearing the simulated shower shapes in case of the SMD multiplicity = 7, which shows the worst agreement between the data and simulation. After the smearing to match the highest shower fraction, the shower width of the simulation also reproduced that of the experimental data. The position resolution increased 14% after the smearing.

3. Performance of the neutron identification

Events within the detector acceptance in $p + p$ collisions were studied with GEANT3 with PYTHIA event generators, and the performance of neutron identification and its reliability were evaluated.

We studied particle species detected in the ZDC with the 5 GeV energy threshold which was required for the ZDC trigger (without the BBC coincidence requirement). In about 92% of events, only a single particle was detected by the ZDC in each $p + p$ collision, mainly photons, neutrons, and protons. Energy distributions for these three particles are plotted in Fig. 8.

Only neutral particles, photons and neutrons were expected to be detected with the ZDC due to sweeping of charged particles by the DX magnet. However, scattered protons could hit the DX magnet or beam pipe and create a hadronic shower, and particles from the shower could hit the ZDC.

Most of the photons and neutrons were generated by diffractive and gluon scattering processes. In PYTHIA hard processes, neutrons are generated mainly from string fragmentation ($\sim$65%) and then decay from Δ^0, Δ^+, Δ^-, Λ^0. The forward photons were generated by decays of π^0s ($\sim$91%) and ηs ($\sim$7%). Protons were generated by

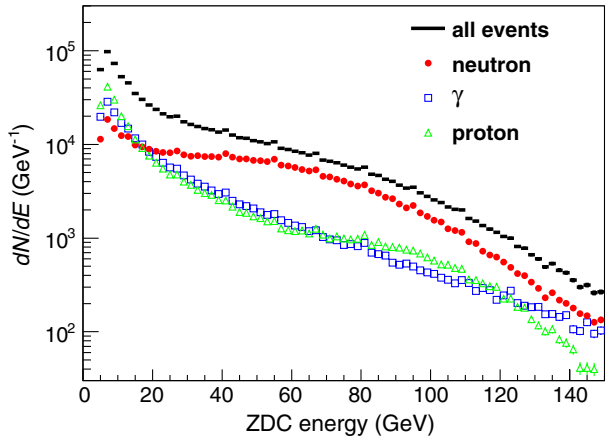

FIG. 8 (color online). Energy distributions in ZDC for neutron, photon, and proton. The ZDC threshold was set at 5 GeV in the ZDC trigger. Events with one particle detected in the ZDC in each $p + p$ collision are shown.

elastic and diffractive processes. Particles depositing less than 20 GeV of energy in the ZDC were predominantly photons and protons as shown in Fig. 8.

Photons are mostly absorbed in the first ZDC module, which is 51 r.l. long. Thus, photons were removed by requiring energy deposited in the SMD or in the second ZDC module. In photon rejection with the SMD, more than one scintillator above threshold (the SMD multiplicity ≥ 2) was required for both x and y. After applying this cut, the neutron purity was estimated to be $93.6 \pm 0.3\%$. In photon rejection with the second ZDC module, energy deposited in the second ZDC module above 20 GeV was required. After applying this cut, the neutron purity was estimated to be $93.6 \pm 0.5\%$. In the analyses of the cross section and the asymmetry, photon rejection with the SMD was applied since the position information calculated by the SMD was required. Rejection with the second ZDC was used for the estimation of the rejection efficiency with the SMD which is discussed in Sec. III A.

The charge veto counter was used to reject protons. A neutron energy above 20 GeV and the charge veto cut removed most proton events, as discussed later in this section.

The main backgrounds after neutron identification are K^0s and protons. The purities were estimated for neutron energies above 20 GeV. In the cross section and the asymmetry analyses, we also required the acceptance cut and/or a higher energy cut. In these cases, the purities improve and are estimated in each analysis section.

In the ISR experiment, the K^0 contamination to the neutron measurement was estimated from the $K^\pm$ measurements [3]. They obtained 10% contamination at $x_F = 0.2$ and less than 4% at $x_F > 0.4$. The fraction of K^0 to neutron in PYTHIA is consistent with the ISR result. We have included no correction for the K^0 contamination in this analysis.

The proton background is very sensitive to the materials around the ZDC and the magnet tuning in the accelerator. The systematic uncertainty of proton contamination was estimated by the simulation using the measured fraction of charged events in the charge veto counter. Noise was estimated by the pedestal width of the data and was incorporated into the simulation. For the proton contamination analysis, photon events were removed by requiring the second ZDC module cut. The fraction of proton events can be estimated as a fraction of charged candidates, which are the events with one more minimum ionization particle in the charge veto counter. These fractions were 0.42 and 0.28 for the data and simulation, respectively. Proton events in the experimental data were about 1.5 times more frequent than that of the simulation. We ascribe the difference to beam conditions that cause interactions with materials around the DX magnet and the ZDC.

The threshold dependence of the selection of charged particle candidates was also studied. The change in the

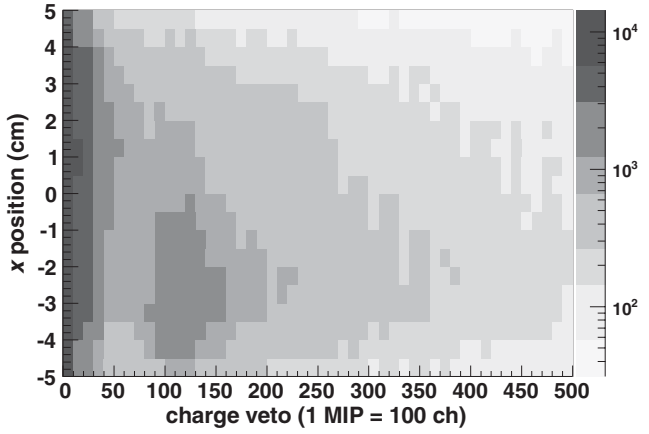

FIG. 9. The x position calculated by the SMD vs the charge distribution in the charge veto counter for the experimental data. Most charged events were distributed in the negative x region which is the direction of beam bending by the DX magnet.

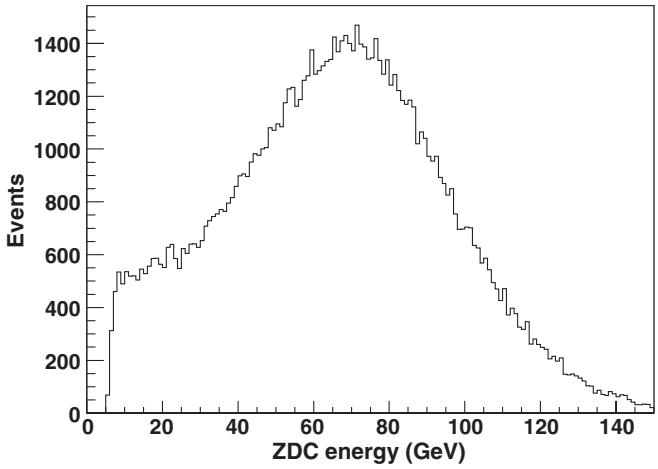

FIG. 10. The energy distribution measured with the ZDC after the neutron identification and the acceptance cut ($r < 2$ cm, corresponds to $p_T < 0.11 \cdot x_F$ GeV$/c$).

charged-particle fraction was less than 1% so that the threshold dependence was negligibly small. Therefore, the factor 1.5 was a reasonable estimate for the fraction of charged candidates between the data and simulation.

The proton background was estimated and included in the systematic uncertainties. According to the simulation study for the structure of proton events, proton events should be detected in the direction of beam bending which is negative x for the south ZDC. This behavior was confirmed by the experimental data as shown in Fig. 9 which is a plot of the x position determined by the SMD vs the charge distribution in the charge veto counter. Most charged candidates were distributed in the negative x region.

III. CROSS SECTION MEASUREMENT

A. Analysis

The differential cross section with respect to x_F was measured:

$$\frac{d\sigma}{dx_F} = \frac{N_{\text{neutron}}}{\mathcal{L}} \frac{1}{dx_F}, \tag{7}$$

where N_{neutron} is the number of neutrons after the correction of cut efficiencies and the energy unfolding.

For the cross section analysis, 6.5 million events taken by the ZDC trigger were used from the sampled luminosity of 240 nb^{-1}. The acceptance cut $r < 2$ cm was used to select kinematics similar to the ISR experiment. We assumed the beam axis was the same as the ZDC center in this analysis, and the deviation was evaluated as a systematic uncertainty. The beam axis compared to the ZDC center is discussed in Appendix A.

Figure 10 shows the energy distribution measured with the ZDC after the neutron identification and the acceptance cut. The energy spectrum was peaked at about 70 GeV, and this was used for a stability check of the ZDC gain run by run, which was found to be stable. The ratio of the neutron yield to the BBC counts without the collision vertex requirement was used for a stability check of the neutron selection, and it was also found to be stable.

One background source was beam-gas interaction. Beam-gas events are normally removed by requiring a forward-backward coincidence of the BBC detectors. However, this could not be done for the ZDC triggered events. Instead, we evaluated the fraction of beam-gas background using the 9 noncolliding bunch crossings with the combination of filled and empty bunches at PHENIX. We found that the fraction was 0.0062 ± 0.0004 on average, negligibly small.

The neutron hit position was calculated by the centroid method using the distribution of scintillator charge above the threshold in the SMD, Eq. (4). In this analysis, the same threshold was applied to the data and simulation, and the efficiency of the SMD cut was estimated by simulation. The difference of efficiencies caused by uncertainty of the SMD cut efficiency was estimated using the nearly pure neutron sample by the neutron identification with the second ZDC cut (Sec. II B 3). The energy spectrum was corrected based on the SMD cut efficiency before the energy unfolding.

The measured neutron energy with the ZDC is smeared by the energy resolution. To extract the initial energy distribution, it is necessary to unfold the measured energy distribution. The energy unfolding method is described in Appendix B.

The ZDC energy response to neutrons below 100 GeV was found by the simulation to be nonlinear as described in Sec. II B 1. This nonlinearity was included in the transition matrix A of Appendix B and corrected by the energy unfolding. Since the hadronic interaction could only be determined from simulation, a systematic uncertainty was included, using the variation of the cross section evaluated with a different matrix A with a linear response.

The efficiency of the experimental cuts, including the neutron identification and the acceptance cut, for the

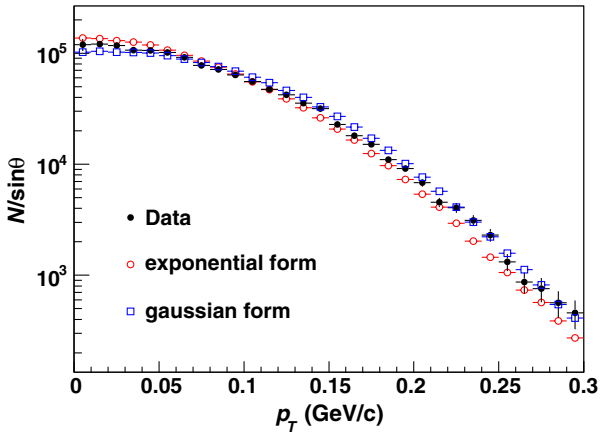

FIG. 11 (color online). Comparison of the p_T distribution from experimental data (black closed circles) and two simulations using Gaussian form (blue open squares) and exponential form (red open circles) inputs.

unfolded x_F distribution was estimated by the simulation with the single neutron event generator. The acceptance cut used the radius, r, and the efficiency was evaluated from the p_T distribution based on Eq. (3): $p_T \approx x_F \cdot E_p \cdot \theta_n \approx 0.056 \cdot x_F \cdot r$ GeV/c.

For the p_T distribution, we used two distributions: a Gaussian form $d\sigma/dp_T \propto \exp(-ap_T^2)$, where $a(x_F)$ was obtained by HERA [11] with error evaluation, and an exponential form $d\sigma/dp_T \propto \exp(-bp_T)$, where $b = 4.8 \pm 0.3(\mathrm{GeV}/c) - 1$ which was used in the ISR analysis [2,3]. The simulated p_T distributions with those two input distribution were compared with experimental data normalized to the same total entries. It was found that the differences between data and those two inputs were not large as shown in Fig. 11.

Figure 12 shows the simulated p_T distributions (dashed line) in each x_F bin. The geometrical maximum p_T for the acceptance cut, $r < 2$ cm, in each x_F is given by $p_T^{\mathrm{Max}} = 0.11 \cdot x_F$ GeV/c, shown as dotted-dashed vertical lines. The actual p_T distributions with the experimental cuts were smeared due to the position resolution and the energy resolution, shown as solid lines. Ratios of these counts

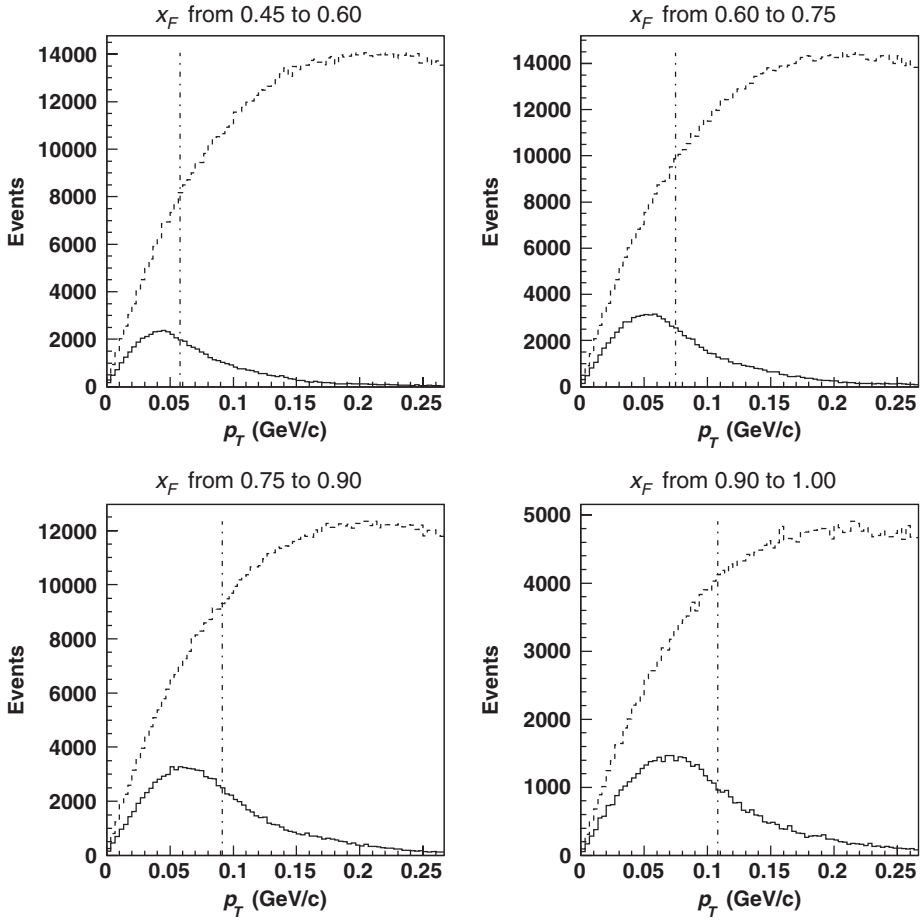

FIG. 12. Simulated p_T distributions using the Gaussian p_T shape. Initial p_T distributions are shown as dashed lines in each x_F region. The expected p_T region for the acceptance, $r < 2$ cm, is below the vertical dotted-dashed lines, which are the maximum p_T calculated as $\approx 0.11 \cdot x_F$ GeV/c. The actual p_T distributions with the experimental cuts are shown as solid lines.

TABLE I. The expected p_T for $r < 2$ cm, mean p_T value with the experimental cut, and the efficiency for the experimental cut estimated by the simulation (Fig. 12). The errors were derived considering the uncertainty in the parameter $a(x_F)$ in the Gaussian form evaluated by HERA.

Neutron x_F	Mean p_T (GeV/c)	Efficiency
0.45–0.60	0.072	$0.779 \pm 0.014(1.8\%)$
0.60–0.75	0.085	$0.750 \pm 0.009(1.2\%)$
0.75–0.90	0.096	$0.723 \pm 0.006(0.8\%)$
0.90–1.00	0.104	$0.680 \pm 0.016(2.3\%)$

are the efficiency for the experimental cuts and are listed in Table I. The errors were derived considering the uncertainty in the parameter $a(x_F)$ in the Gaussian form evaluated by HERA. There is no significant difference in the result in case of using the ISR (exponential) p_T distribution.

The mean values of the simulated p_T distributions in each energy region are also listed in Table I. The cross section was obtained after the correction of the energy unfolding and the cut efficiency.

Table II summarizes all systematic uncertainties evaluated as the ratio of the variation to the final cross section values. The absolute normalization error is not included in these errors. It was estimated by BBC counts to be 9.7% (22.9 ± 2.2 mb for the BBC trigger cross section).

The background contamination in the measured neutron energy with the ZDC energy from 20 to 140 GeV for the acceptance cut of $r < 2$ cm was estimated by the simulation with the PYTHIA event generator. The background from protons was estimated to be 2.4% in the simulation. The systematic uncertainty in the experimental data was determined to be 1.5 times larger than this as discussed in Sec. II B 3. Multiple particle detection in each collision was estimated to be 7% with the $r < 2$ cm cut.

In the cross section analysis, we evaluated the beam center shift described in Appendix A as a systematic uncertainty. For the evaluation, cross sections were calculated in the different acceptances according to the result of the beam center shift while requiring $r < 2$ cm, and the variations were applied as a systematic uncertainty.

TABLE II. Systematic uncertainties for the cross section measurement. The absolute normalization error is not included in these errors. The absolute normalization uncertainty was estimated by BBC counts to be 9.7% (22.9 ± 2.2 mb for the BBC trigger cross section).

	Exponential p_T form		Gaussian p_T form
p_T distribution	3%–10%		7%–22%
Beam center shift		3%–31%	
Proton background		3.6%	
Multiple hit		7%	
Total	11%–33%		16%–39%

TABLE III. The result of the differential cross section $d\sigma/dx_F$(mb) for neutron production in $p + p$ collisions at $\sqrt{s} = 200$ GeV. The first uncertainty is statistical, after the unfolding, and the second is the systematic uncertainty. The absolute normalization error, 9.7%, is not included.

$\langle x_F \rangle$	Exponential p_T form	Gaussian p_T form
0.53	$0.243 \pm 0.024 \pm 0.043$	$0.194 \pm 0.021 \pm 0.037$
0.68	$0.491 \pm 0.039 \pm 0.052$	$0.455 \pm 0.036 \pm 0.085$
0.83	$0.680 \pm 0.044 \pm 0.094$	$0.612 \pm 0.044 \pm 0.096$
0.93	$0.334 \pm 0.035 \pm 0.111$	$0.319 \pm 0.037 \pm 0.123$

B. Result

The differential cross section, $d\sigma/dx_F$, for forward neutron production in $p + p$ collisions at $\sqrt{s} = 200$ GeV was determined using two p_T distributions: a Gaussian form, as used in HERA analysis, and an exponential form, used for ISR data analysis. The results are listed in Table III and plotted in Fig. 13. We show the results for x_F above 0.45 since the data below 0.45 are significantly affected by the energy cutoff before the unfolding. The p_T range in each x_F bin is $0 < p_T < 0.11 x_F$ GeV/c from Eq. (2) with the acceptance cut of $r < 2$ cm. The absolute normalization uncertainty for the PHENIX measurement, 9.7%, is not included.

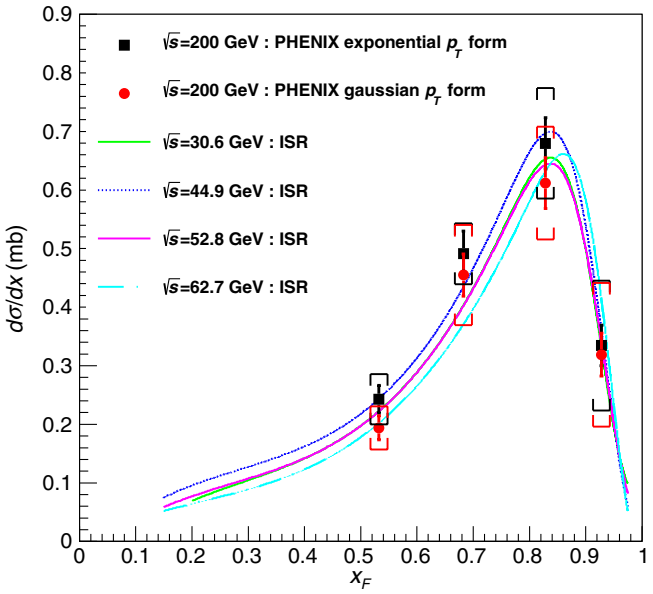

FIG. 13 (color online). The cross section results for forward neutron production in $p + p$ collisions at $\sqrt{s} = 200$ GeV are shown. Two different forms, exponential (squares) and Gaussian (circles), were used for the p_T distribution. Statistical uncertainties are shown as error bars for each point, and systematic uncertainties are shown as brackets. The integrated p_T region for each bin is $0 < p_T < 0.11 x_F$ GeV/c. Shapes of ISR results are also shown. Absolute normalization errors for the PHENIX and ISR are 9.7% and 20%, respectively.

Invariant cross sections measured at the ISR experiment were converted to differential cross sections for the comparison with the PHENIX data. The conversion formula from the invariant cross section $Ed^3\sigma/dp^3$ to $d\sigma/dx_F$ is described with the approximation in the forward kinematics as

$$\frac{d\sigma}{dx_F} = \frac{2\pi}{x_F}\int_{\mathrm{Acc}} E\frac{d^3\sigma}{d^3p}p_T dp_T, \tag{8}$$

where Acc. means the p_T range of the PHENIX acceptance cut; $0 < p_T < 0.11x_F$ GeV/c for the $r < 2$ cm cut. As a p_T shape, we used an exponential form $\exp(-4.8p_T)$ which was obtained from the $0.3 < x_F < 0.7$ region from the ISR results [2,3].

For both Table III and Fig. 13, we give the PHENIX results for two p_T shapes, the exponential shape used for the ISR results, and the Gaussian shape used for HERA results.

The measured cross section at $\sqrt{s} = 200$ GeV is consistent with the ISR result, indicating that x_F scaling is satisfied at the higher center of mass energy. This result is consistent with the OPE model [4–10].

IV. SINGLE TRANSVERSE SPIN ASYMMETRY MEASUREMENT

A. Analysis

The single transverse spin asymmetry is obtained from the azimuthal modulation of neutron production relative to the polarization direction of a transversely polarized beam on an unpolarized target and normalized by an independent measurement of the beam polarization. The stable polarization direction of protons is vertical with respect to the accelerator plane. There is an approximately equal number of bunches filled with the spin of polarization-up protons as of polarization-down protons. With both beams polarized, single-spin analyses were performed by taking into account the polarization states of one beam, averaging over those of the other. The beam polarizations were measured using fast carbon target polarimeters [18] at a different location at RHIC with several measurements in each fill. The carbon target measurements were normalized to absolute polarization measurements made by a separate polarized atomic hydrogen jet polarimeter [19]. The polarizations ranged from 0.43 to 0.48 for the blue beam and from 0.46 to 0.52 for the yellow beam. Systematic uncertainty for the blue beam polarization is 5.9%, and that for the yellow beam polarization is 6.2%.

The acceptance cut at the ZDC required $0.5 < r < 4.0$ cm. We used an $r < 4.0$ cm cut for the x_F-integrated asymmetry analysis in order to obtain maximum statistics, where the uncertainty from background contamination was canceled out. We also applied a 0.5 cm $< r$ cut in order to avoid a smearing effect of the left-right separation around $r = 0$ by the position resolution. We used an $r < 3.0$ cm cut for x_F-dependence analysis of the asymmetry. We applied a tighter cut in the x_F-dependence analysis for better control of the background contamination for smaller statistics in each x_F bin. Figure 14 shows p_T distributions for each cut in the ZDC trigger and the ZDC ⊗ BBC trigger.

The acceptance definition for the azimuthal angle (ϕ) of neutron production is shown in Fig. 15, where the polarization-up direction points to $\phi = 0$. The acceptance area was divided into 16 slices in a radial pattern. For the asymmetry calculation, we used a square-root formula which cancels many systematic uncertainties, such as detector and luminosity asymmetries:

$$\epsilon_N(\phi) = \frac{\sqrt{N^{\uparrow}_{\phi}N^{\downarrow}_{\phi+\pi}} - \sqrt{N^{\uparrow}_{\phi+\pi}N^{\downarrow}_{\phi}}}{\sqrt{N^{\uparrow}_{\phi}N^{\downarrow}_{\phi+\pi}} + \sqrt{N^{\uparrow}_{\phi+\pi}N^{\downarrow}_{\phi}}}, \tag{9}$$

where $N^{\uparrow}_{\phi}$ ($N^{\downarrow}_{\phi}$) is the number of events with polarization-up (-down) producing neutrons to azimuthal angle ϕ.

A correction C_{ϕ} is applied, discussed later, to account for smearing from position resolution. After normalization by the polarization, P, we obtain the asymmetry as

$$\mathcal{A}(\phi) = \frac{1}{P}\frac{1}{C_{\phi}}\epsilon_N(\phi). \tag{10}$$

For this analysis, we used 6.5 million and 17.6 million events for the ZDC trigger sample and ZDC ⊗ BBC trigger sample, respectively, from the sampled luminosity of

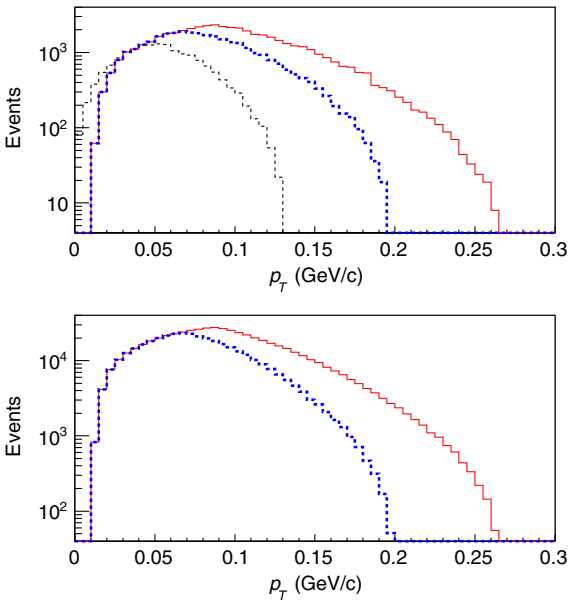

FIG. 14 (color online). p_T distributions for the (solid [red] line) $0.5 < r < 4.0$ cm cut and (thick dotted [blue] line) $0.5 < r < 3.0$ cm cut used for asymmetry analysis in the (upper) ZDC trigger and (lower) ZDC ⊗ BBC trigger. Also shown for the (upper) ZDC trigger are the (thin dashed [black] line) p_T distributions for the $r < 2.0$ cm cut used for cross section analysis.

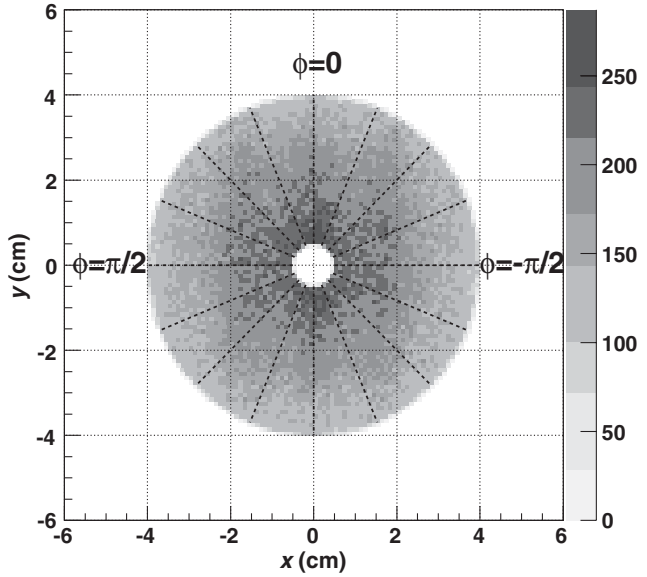

FIG. 15. The acceptance definition for the ϕ dependence of ϵ_N, shown as a plot of the measured neutron position at the ZDC. The acceptance was divided into 16 slices in a radial pattern, and the asymmetry was calculated by the square root formula from $\phi = -\pi/2$ to $\pi/2$.

240 nb^{-1}. A ZDC energy cut was required to select 40–120 GeV in the measured energy.

The raw measured asymmetry $\epsilon_N(\phi)$ divided by the polarization are fitted to a sine:

$$\mathcal{A}(\phi) = A_N \sin(\phi - \phi_0), \tag{11}$$

where ϕ_0 allows a deviation of the maximum asymmetry axis from vertical.

In the present analysis, we used only the south ZDC detector, which faces the yellow beam. The forward neutron asymmetry uses the polarized yellow beam and sums over the polarization states of the blue beam bunches. Following the Basel (Ann Arbor) Convention [20], a positive A_N indicates more production to the left of the polarized (yellow) beam, for the polarization-up bunches in the yellow beam. The asymmetry for neutrons produced backward was measured using a polarized blue beam, summing over the polarization states of the yellow beam bunches. In order to follow the Basel Convention, signs of the backward A_N were inverted from the fitting results. A positive A_N would indicate more neutron production to the left of the blue (polarized) beam for polarization-up bunches.

We performed two sets of simulations to estimate the smearing parameters, C_ϕ, which were correlated to the neutron energy-dependent position resolution (Sec. II B 1). The energy distributions for the simulation inputs were determined in the same way as the cross section analysis (Sec. III A).

The $\epsilon_N(\phi)$ was smeared from the $\mathcal{A}(\phi)$ due to position resolution. From Eq. (10), the smearing parameter, C_ϕ, can be evaluated from simulation as

$$C_\phi = \frac{A_N^{\text{Output}}}{A_N^{\text{Input}}}, \tag{12}$$

where A_N^{Output} corresponds to the $\epsilon_N(\phi)$ of the experimental data; it includes effects of the experimental cut and the position resolution. As A_N^{Input}, we generated neutrons with the sine modulated $\mathcal{A}(\phi)$ as Eq. (11) with $A_N = A_N^{\text{Input}} = -0.10$. The smeared amplitude was obtained as $A_N^{\text{Output}} = -0.076$, and their ratio, 0.76, is the correction factor of the smearing effect, $C_\phi = 0.760 \pm 0.015$ (ZDC trigger). For the ZDC ⊗ BBC trigger, we obtained the smearing parameter $C_\phi = 0.746 \pm 0.016$ (ZDC ⊗ BBC trigger).

For the analysis of the x_F dependence of A_N, we chose bins of 40–60, 60–80, and 80–120 GeV in the measured ZDC energy. Events with ZDC energy greater than 120 GeV were eliminated from this analysis (3.8% of the events). Similar simulations and calculations of C_ϕ were performed for the analysis of the x_F dependence of the asymmetry with both the ZDC trigger and ZDC ⊗ BBC trigger.

After correction for the smearing effect, we obtain the measured energy dependence of A_N. The mean x_F values for the ZDC trigger sample and ZDC ⊗ BBC trigger sample were evaluated by the simulations which were modified to reproduce the measured energy distributions for each trigger sample.

The background contamination was studied by the simulation with the PYTHIA event generator. In the analysis of the x_F dependence of A_N, an acceptance cut of $r < 3$ cm was applied.

After the neutron identification and the acceptance cut, as described in Sec. II B 3, the neutron purities were 0.975 ± 0.006 for the ZDC trigger sample and 0.977 ± 0.010 for ZDC ⊗ BBC trigger sample. Main background contributions were the K^0 and proton. According to the discussion in Sec. II B 3, we applied the systematic uncertainty contributed from the proton only.

The A_N of the proton background was evaluated by calculating A_N of the neutral sample and charged sample defined by using the charged veto counter in front of the ZDC. For each sample, we evaluated the fraction of the neutral-particle component and the charged-particle component with the PYTHIA simulation and calculated A_N of neutral-particle and charged-particle components. By comparing A_N of the neutral-particle component and the neutral sample (mainly neutron), we evaluated background from A_N of charged particles (mainly proton).

For ZDC trigger events, the systematic uncertainty from the proton background was evaluated to be 3.1%. For ZDC ⊗ BBC trigger events, it was evaluated to be 1.1%. They were increased by the factor 1.5 estimated higher frequency of proton background in the experimental data, compared to simulation, to give 4.7% and 1.7%, which were included as systematic uncertainties.

Multiple particle detection in each collision was estimated to be 6.5% for the ZDC trigger and 5.9% for the ZDC ⊗ BBC trigger for the $0.5 < r < 4.0$ cm cut.

To evaluate the systematic uncertainty for determination of the beam axis, A_N were calculated with center positions as $(x, y) = (0.46, 0.00)$, $(0.00, -1.10)$, and $(0.46, -1.10)$ cm while keeping the acceptance cut, $0.5 < r < 4.0$ cm. These values were chosen based on measurements of the beam center as discussed in Appendix A. Maximum variations to final values, which were calculated by $(x, y) = (0.00, 0.00)$ cm, were included as systematic uncertainties.

Since the smearing effect was caused by the position resolution, the systematic uncertainty of the position resolution, 14% (Sec. II B 2), should be reflected in the uncertainties for the result. This was evaluated with a variation of the asymmetry calculated with 14% increased position resolution uncertainty in the simulation. The asymmetry was reduced by 4.2%. This was assigned as a systematic uncertainty of the smearing correction.

A technique called "bunch shuffling" was used to check for systematic effects in the asymmetry measurements due to a variation of beam characteristics bunch by bunch. By randomly assigning bunch polarization directions, we create data sets of experimental data with little or no net polarization and compare the resulting measured asymmetry with statistical uncertainties. The fluctuation of measured asymmetries should correspond to the statistical uncertainty. We concluded that the fake asymmetry from bunch characteristics is less than $0.39\sigma_{\text{stat}}$ and $0.36\sigma_{\text{stat}}$ for the ZDC trigger and ZDC ⊗ BBC trigger, respectively. We do not include these uncertainties in the final systematic uncertainties for A_N.

p_T-correlated uncertainties from the beam center shift were evaluated in a similar way to the cross section analysis described in Appendix A. They were 0.004 in the x_F-integrated analysis and 0.004–0.010 in the x_F-dependent analysis.

Scale uncertainties are summarized in Table IV for the A_N measurements. Values are presented as scale variations to the final values. Total uncertainties were calculated by the quadratic sum. The scale uncertainty from the beam polarization is not included in the table. The uncertainty in the yellow beam polarization which was used in the forward neutron asymmetry measurement was ±6.2%, and that in the blue beam polarization used in the backward neutron asymmetry measurement was ±5.9%.

TABLE IV. Scale uncertainties for the A_N measurements.

	ZDC trigger	ZDC ⊗ BBC trigger
Proton background	4.7%	1.7%
Multiple hit	6.5%	5.9%
Smearing	4.2%	
Total	9.1%	7.4%

B. Azimuthal modulation of forward neutron production

In this section we present the results for the azimuthal modulations for neutron production, within the acceptance from $\theta_n = 0.3$ mrad ($r = 0.5$ cm at ZDC) to $\theta_n = 2.2$ mrad ($r = 4$ cm) and ZDC energy from 40 to 120 GeV.

Asymmetries $\mathcal{A}(\phi)$ were calculated for eight azimuthal angle bins, using Eqs. (9) and (10). Figures 16 and 17 present $\mathcal{A}(\phi)$ for the two trigger conditions, for forward and backward neutron production, respectively. Statistical uncertainties are shown, but the p_T-correlated systematic uncertainties from the beam center shift are not shown. In addition, there are scale uncertainties listed in Table IV and polarization scale uncertainties.

A significant asymmetry is present for forward neutron production. The $\mathcal{A}(\phi)$ data were fitted with a sine curve, Eq. (11), to obtain A_N. The azimuthal offsets, ϕ_0, were consistent with $\phi_0 = 0$. The results obtained for A_N are: $A_N = -0.061 \pm 0.010(\text{stat}) \pm 0.004(\text{syst})$ [$\chi^2/\text{ndf} = 3.05/6$] for the ZDC trigger sample and $A_N = -0.075 \pm 0.004(\text{stat}) \pm 0.004(\text{syst})$ [$\chi^2/\text{ndf} = 2.22/6$] for the ZDC ⊗ BBC trigger sample. There is no observed asymmetry for backward neutron production. The results for backward neutron production for A_N are: $A_N = -0.006 \pm 0.011(\text{stat}) \pm 0.004(\text{syst})$ [$\chi^2/\text{ndf} = 5.18/6$] for the ZDC

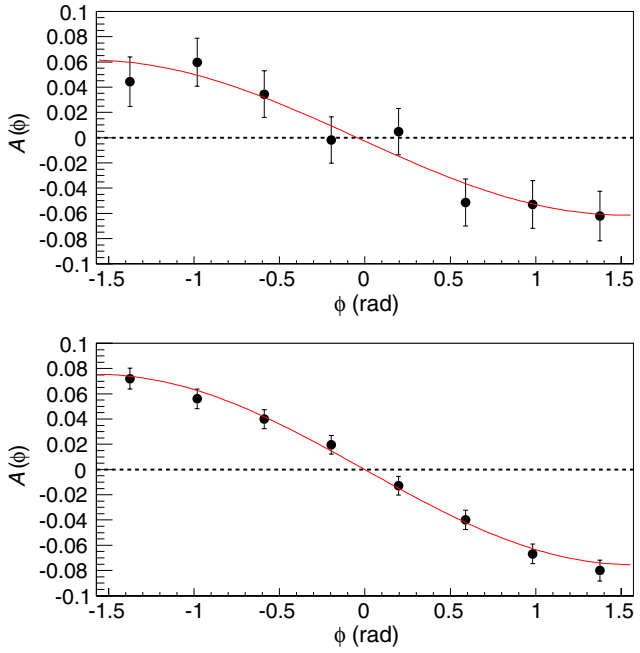

FIG. 16 (color online). Results for the azimuthal modulation for forward neutron production from polarized $p + p$ collisions at $\sqrt{s} = 200$ GeV in the (upper) ZDC trigger sample and the (lower) ZDC ⊗ BBC trigger sample. The error bars indicate the statistical uncertainties. Results for a $\sin(\phi)$ fit to the data are indicated. The p_T-correlated systematic uncertainties from the beam center shift and scale uncertainties listed in Table IV and polarization scale uncertainties are not included.

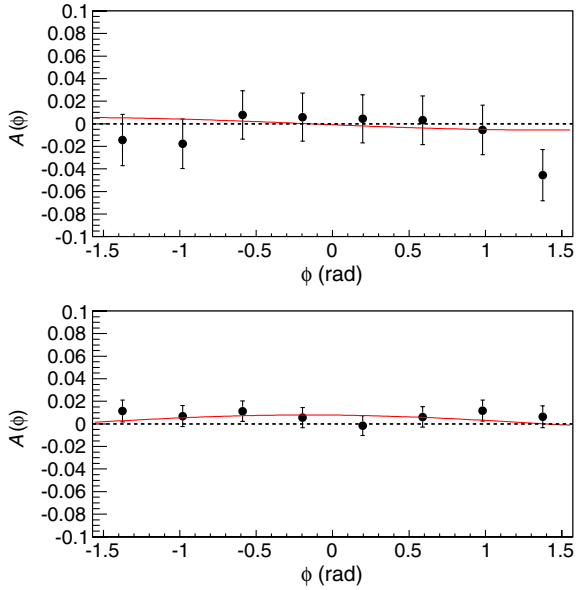

FIG. 17 (color online). Results for the azimuthal modulation for backward neutron production from polarized $p+p$ collisions at $\sqrt{s}=200$ GeV in the (upper) ZDC trigger sample and the (lower) ZDC ⊗ BBC trigger sample. The error bars indicate the statistical uncertainties. Results for a $\sin(\phi)$ fit to the data are indicated. The p_T-correlated systematic uncertainties from the beam center shift and scale uncertainties listed in Table IV and polarization scale uncertainties are not included.

trigger sample and $A_N = -0.008 \pm 0.005(\text{stat}) \pm 0.004(\text{syst})$ [$\chi^2/\text{ndf} = 3.31/6$] for the ZDC ⊗ BBC trigger sample.

To compare with the previous result [1] from the polarimeter development experiment at RHIC, we compared to the A_N of the forward ZDC ⊗ BBC trigger sample. The amplitude of the measured A_N was $A_N = (-0.090 \pm 0.006 \pm 0.009) \times (1.00^{+0.52}_{-0.25})$. Errors indicate the statistics, systematics, and the scaling uncertainty from the polarization measurement. The two results are consistent within the errors, including the scaling uncertainties. We note that the two measurements used slightly different detection coverages for the charged particle interaction trigger: $2.2 < |\eta| < 3.9$ in the horizontal and vertical directions for the polarimeter development experiment and $3.0 < |\eta| < 3.9$ for the PHENIX experiment.

C. x_F dependence of A_N

The x_F dependence of A_N for production is listed in Tables V and VI and plotted in Fig. 18. The $\mathcal{A}(\phi)$ data were fitted with a sine curve, Eq. (11), to obtain A_N with $\phi_0 = 0$. The mean x_F values were determined according to Sec. IV A. Statistical uncertainties are shown as error bars, and p_T-correlated systematic uncertainties are shown as brackets. Scale uncertainties from the asymmetry measurements and the beam polarization are not included.

We observe significant negative A_N for neutron production in the positive x_F region and with no energy dependence within the uncertainties, both for inclusive neutron production and for production including a beam-beam interaction requirement. No significant backward neutron production asymmetry is observed.

TABLE V. The results of the x_F dependence of A_N for neutron production in the ZDC trigger sample of $p+p$ collisions at $\sqrt{s}=200$ GeV. First and second uncertainties show statistical and p_T-correlated systematic uncertainties, respectively. Scale uncertainties from the asymmetry measurements and the beam polarization are not included.

$\langle x_F \rangle$	A_N	χ^2/ndf
−0.776	$-0.0059 \pm 0.0252 \pm 0.0095$	11.6/7
−0.682	$-0.0219 \pm 0.0255 \pm 0.0035$	6.833/7
−0.568	$-0.0050 \pm 0.0303 \pm 0.0076$	9.252/7
0.568	$-0.0503 \pm 0.0263 \pm 0.0076$	7.012/7
0.682	$-0.0625 \pm 0.0221 \pm 0.0035$	2.68/7
0.776	$-0.0772 \pm 0.0217 \pm 0.0095$	5.38/7

TABLE VI. The results of the x_F dependence of A_N for neutron production in the ZDC ⊗ BBC trigger sample of $p+p$ collision at $\sqrt{s}=200$ GeV. First and second uncertainties show statistical and p_T-correlated systematic uncertainties, respectively. Scale uncertainties from the asymmetry measurements and the beam polarization are not included.

$\langle x_F \rangle$	A_N	χ^2/ndf
−0.749	$0.0035 \pm 0.0117 \pm 0.0082$	2.672/7
−0.664	$-0.0093 \pm 0.0106 \pm 0.0037$	2.915/7
−0.547	$-0.0033 \pm 0.0115 \pm 0.0096$	6.783/7
0.547	$-0.0629 \pm 0.0097 \pm 0.0096$	13.27/7
0.664	$-0.0657 \pm 0.0090 \pm 0.0037$	5.425/7
0.749	$-0.0667 \pm 0.0099 \pm 0.0082$	5.003/7

V. DISCUSSION

The measurement of the cross section for the $p+p$ production of neutrons at $\sqrt{s}=200$ GeV has been presented here, and it is consistent with x_F scaling when compared to ISR results. These cross sections are described by the OPE model in Regge calculus [4–10]. Therefore, the observed large asymmetry for neutron production at RHIC, as presented in Ref. [1] and here, may arise from the interference between a spin-flip amplitude due to the pion exchange and nonflip amplitudes from other Reggeon exchanges. So far our knowledge of Reggeon exchange components for neutron production is limited to the pion. Under the OPE interpretation, the asymmetry has sensitivity to the contribution of all spin nonflip Reggeon exchanges, even if the amplitudes are small. Recently Kopeliovich *et al.* calculated the A_N of forward neutron production from the interference of pion and Reggeon exchanges, and the results were in good agreement with the PHENIX data [21].

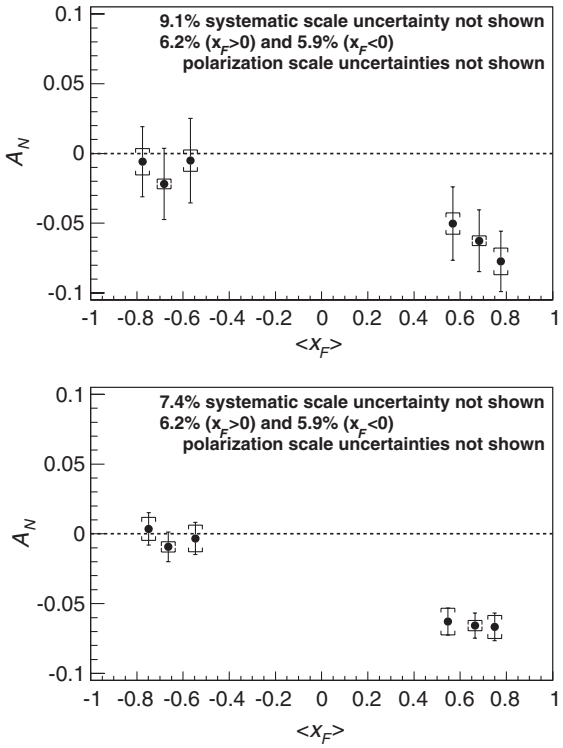

FIG. 18. The x_F dependence of A_N for neutron production in the (upper) ZDC trigger sample and for the (lower) ZDC ⊗ BBC trigger sample. The error bars show statistical uncertainties, and brackets show p_T-correlated systematic uncertainties. Systematic scale uncertainties listed in Table IV and polarization scale uncertainties are not included.

We can also discuss our results based on the meson-cloud model [22]. This model gives a good description for the result from a Drell-Yan experiment at FNAL, E866 [23]. In this model, the Drell-Yan process is generated by the interaction between the d quark in one proton and the $\bar{d}$ quark in the π^+ of the $p \rightarrow n\pi^+$ state for the other proton. In this model the neutron should be generated with very forward kinematics, possibly similar to the kinematics of the results presented here. The meson-cloud model was successfully applied to neutron production in the ISR experiment [8], and we expect it is applicable to our A_N and cross section measurements for higher energy $p + p$ collisions.

VI. CONCLUSION

We have measured the cross section and single transverse spin asymmetry, A_N, for very forward neutron production in polarized $p + p$ collisions at $\sqrt{s} = 200$ GeV. The results from the PHENIX experiment at RHIC were based on a ZDC augmented by a shower maximum detector, covering neutron production angles to $\theta_n = 2.2$ mrad. A large A_N for neutron production had been observed in a polarimeter development experiment at RHIC, using an electromagnetic calorimeter to identify neutrons, with coarse neutron energy resolution [1]. The PHENIX experiment then outfitted existing ZDC detectors to act as polarimeters to monitor the beam polarizations and polarization directions at the experiment. The results presented here are based on studies with the ZDC polarimeter, which, due to a much better measurement of the neutron energy, provide first measurements of the neutron production cross section at RHIC energy and the dependence of A_N on the neutron energy.

The measured cross section is consistent with x_F scaling from ISR results. Within uncertainties, the observed A_N were consistent with the previous result at RHIC [1], and for $x_F > 0.45$ (the region measured by this experiment) no significant x_F dependence was observed. We also present measured A_N for neutrons produced backward from the polarized beam. These results are consistent with zero.

The cross sections for large x_F neutron production, as well as those in $e + p$ collisions at HERA, are largely reproduced by a OPE. Using this model, the observed large asymmetry for the neutron production would be considered to come from the interference between a spin-flip amplitude due to the pion exchange and nonflip amplitudes from other Reggeon exchanges. On the basis of the OPE model, the large neutron A_N would have sensitivity to the contribution of other Reggeon exchanges.

Future measurements of neutron production cross sections and asymmetries will include analysis of the RHIC runs at $\sqrt{s} = 62.4$ GeV and at 500 GeV. The measurements at different center of mass energies will probe the x_F and p_T dependence for neutron production at fixed, very forward production angles $\theta_n < 2.2$ mrad.

ACKNOWLEDGMENTS

We thank the staff of the Collider-Accelerator and Physics Departments at Brookhaven National Laboratory and the staff of the other PHENIX participating institutions for their vital contributions. We acknowledge support from the Office of Nuclear Physics in the Office of Science of the Department of Energy; the National Science Foundation, a sponsored research grant from Renaissance Technologies LLC; Abilene Christian University Research Council; Research Foundation of SUNY; dean of the College of Arts and Sciences, Vanderbilt University (USA); Ministry of Education, Culture, Sports, Science, and Technology and the Japan Society for the Promotion of Science (Japan); Conselho Nacional de Desenvolvimento Científico e Tecnológico and Fundação de Amparo à Pesquisa do Estado de São Paulo (Brazil); Natural Science Foundation of China (People's Republic of China); Ministry of Education, Youth and Sports (Czech Republic); Centre National de la Recherche Scientifique, Commissariat à l'Énergie Atomique, and Institut National de Physique Nucléaire et de Physique des Particules (France); Bundesministerium für Bildung und Forschung,

Deutscher Akademischer Austausch Dienst, and Alexander von Humboldt Stiftung (Germany); Hungarian National Science Fund, OTKA (Hungary); Department of Atomic Energy and Department of Science and Technology (India); Israel Science Foundation (Israel); National Research Foundation and WCU program of the Ministry Education Science and Technology (Korea); Ministry of Education and Science, Russian Academy of Sciences, Federal Agency of Atomic Energy (Russia); VR and Wallenberg Foundation (Sweden); the U.S. Civilian Research and Development Foundation for the Independent States of the Former Soviet Union; the US-Hungarian Fulbright Foundation for Educational Exchange; and the US-Israel Binational Science Foundation.

APPENDIX A: THE STUDY OF THE BEAM AXIS ON THE DETECTOR GEOMETRY

The ZDC center was aligned to the beam axis at the beginning of the 2003 run. We assumed that the beam axis was on the ZDC center in this analysis of 2005 data. We used two approaches to estimate the beam and ZDC alignment. Peripheral neutrons from a heavy ion run just prior to the polarized proton run gave centers of $x = 0.28 \pm 0.01$ cm and $y = -0.07 \pm 0.01$ cm at the south ZDC. The center of the asymmetry A_N was also used to determine the center of the beam axis at the ZDC, since A_N must be zero at zero production angle. We used the ZDC ⊗ BBC trigger sample in this analysis. The asymmetry was measured for a vertically polarized beam to obtain the center in x and for a special run with horizontally polarized beam to obtain the center in y. The results were $x = +0.46 \pm 0.08$ cm and $y = -1.10 \pm 0.14$ cm. The results of the two techniques agreed reasonably for x and did not agree for y.

The beam axis shifts that we observed were considered as systematic uncertainties for the results. The uncertainties were determined from variations of the cross section and asymmetry obtained by moving the center of acceptance while keeping the same cut region (for example, $r < 2$ cm for the cross section analysis).

APPENDIX B: ENERGY UNFOLDING

The measured neutron energy with the ZDC is smeared by the energy resolution. For the extraction of the original energy distribution, it is necessary to unfold the measured energy distribution. We use an unfolding method proposed in Ref. [24].

We assume that the initial distribution $x(E)$ is smeared to the measured distribution $y(E')$, and this smearing is described by a linear combination. Their relation can be given by a transition matrix $A(E', E)$ as

$$y(E') = A(E', E)x(E) \tag{B1}$$

or $\vec{y} = A\vec{x}$.

If the smearing effect is large, the result is very sensitive to a small change of A. It can be discussed using an orthogonal decomposition. The matrix A is diagonalized into D with a transformation matrix U,

$$\vec{c} = D\vec{b}, \tag{B2}$$

where $D = U^{-1}AU$, and $\vec{c} = U^{-1}\vec{y}$ and $\vec{b} = U^{-1}\vec{x}$ are new vectors transformed from $\vec{y}$ and $\vec{x}$, respectively. The diagonal elements of the matrix D are the eigenvalues λ_j of the matrix A. Each of the coefficients b_j and c_j in $\vec{c} = D\vec{b}$ is transformed independently of any other coefficient by using eigenvalue λ_j,

$$c_j = \lambda_j \cdot b_j. \tag{B3}$$

In order to perform the unfolding, the coefficients c_j have been affected by statistical fluctuations of the elements of the measured vector $\vec{y}$. The b_j which includes the information of initial vector x is obtained by $b_j = c_j/\lambda_j$. The statistical fluctuation of the c_j amplified in the case of small eigenvalue λ_j, resulting in instability. A reasonable result can be obtained by cutting the c_j which has a large statistical uncertainty.

First, the coefficients c_j were calculated. Three sets of the transition matrix A, which have the same energy resolution but different initial energy distributions, were prepared with a simulation to check the statistical error propagation of the c_j. Initial shapes were prepared to increase, be flat, and decrease as a function of x_F. These shapes are close to the cross sections at $p_T \approx 0.0$ GeV/c, 0.2 GeV/c and 0.4 GeV/c in the ISR results. Energy spectra before and after the unfolding are plotted in Fig. 19. The horizontal axis is changed to x_F by Eq. (2).

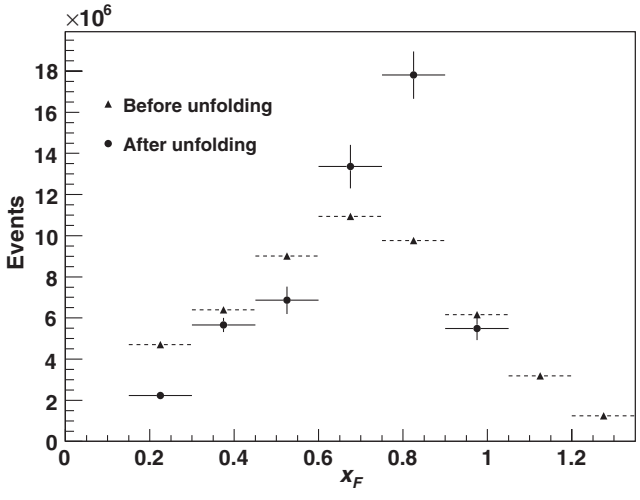

FIG. 19. Energy distributions before and after the energy unfolding. The unfolding was performed so that statistics was conserved.

[1] Y. Fukao *et al.*, Phys. Lett. B **650**, 325 (2007).
[2] J. Engler *et al.*, Nucl. Phys. **B84**, 70 (1975).
[3] W. Flauger and F. Monnig, Nucl. Phys. **B109**, 347 (1976).
[4] A. Capella, J. Tran Thanh Van, and J. Kaplan, Nucl. Phys. **B97**, 493 (1975).
[5] B. Kopeliovich, B. Povh, and I. Potashnikova, Z. Phys. C **73**, 125 (1996).
[6] N. N. Nikolaev, J. Speth, and B. G. Zakharov, arXiv:hep-ph/9708290.
[7] N. N. Nikolaev, W. Schafer, A. Szczurek, and J. Speth, Phys. Rev. D **60**, 014004 (1999).
[8] U. D'Alesio and H. J. Pirner, http://link.springer.com/article/10.1007/s100500050018.
[9] A. B. Kaidalov, V. A. Khoze, A. D. Martin, and M. G. Ryskin, Eur. Phys. J. C **47**, 385 (2006).
[10] A. Bunyatyan and B. Povh, Eur. Phys. J. A **27**, 359 (2006).
[11] S. Chekanov *et al.* (ZEUS Collaboration), Nucl. Phys. **B776**, 1 (2007).
[12] F. D. Aaron *et al.* (H1 Collaboration), Eur. Phys. J. C **68**, 381 (2010).
[13] T. Anticic *et al.* (NA49 Collaboration), Eur. Phys. J. C **65**, 9 (2010).
[14] K. Adcox *et al.* (PHENIX Collaboration), Nucl. Instrum. Methods Phys. Res., Sect. A **499**, 469 (2003).
[15] C. Adler, A. Denisov, E. Garcia, M. J. Murray, H. Strobele, and S. N. White, Nucl. Instrum. Methods Phys. Res., Sect. A **470**, 488 (2001).
[16] R. Brun, F. Carminati, and S. Giani, Report No. CERN-W5013.
[17] T. Sjostrand, P. Eden, C. Friberg, L. Lonnblad, G. Miu, S. Mrenna, and E. Norrbin, Comput. Phys. Commun. **135**, 238 (2001).
[18] O. Jinnouchi *et al.*, RHIC/CAD Accelerator Physics Note 171, 2004.
[19] H. Okada *et al.*, Phys. Lett. B **638**, 450 (2006).
[20] J. Ashkin, E. Leader, M. L. Marshak, J. B. Roberts, J. Soffer, and G. H. Thomas, AIP Conf. Proc. **42**, 142 (1978).
[21] B. Z. Kopeliovich, I. K. Potashnikova, I. Schmidt, and J. Soffer, Phys. Rev. D **84**, 114012 (2011).
[22] K. G. Boreskov and A. B. Kaidalov, Eur. Phys. J. C **10**, 143 (1999); R. J. Fries and A. Schafer, Phys. Lett. B **443**, 40 (1998).
[23] R. S. Towell *et al.* (FNAL E866/NuSea Collaboration), Phys. Rev. D **64**, 052002 (2001).
[24] V. Blobel, arXiv:hep-ex/0208022.